(Received 18 September 2025, Accepted 15 October 2025, Scheduled 26 October 2025)

Broadband Full Functional Reconfigurable Polarization Converter Based on Active Metasurface

Ke Wang[1,2], Chao Zhang[3,4], Wei Li[3,4,*], Jun Fan[1,2], Chuan Shao[1,2], Yi Chao Zhou[1,2], and Shi Jie Xie[1,2]

[1]*School of Information Engineering, Jiangsu College of Engineering and Technology, Nantong, China*
[2]*Nantong Key Laboratory of Artificial Intelligence New Quality Technology Jiangsu College of Engineering and Technology, Nantong, China*
[3]*State Key Laboratory of Millimeter Waves, Southeast University, Nanjing, China*
[4]*School of Information Science and Engineering, Southeast University, Nanjing, China*

ABSTRACT: This article proposes a novel polarization-reconfigurable metasurface converter with multi-functional operation capabilities for flexible polarization manipulation of electromagnetic waves. By integrating PIN diodes into a strategically designed unit cell, the converter achieves dynamic switching among all fundamental polarization conversion modes, including linear-to-linear (co- and cross-polarization), circular-to-circular (co- and cross-polarization), linear to circular polarization (LP-CP), and circular to linear polarization (CP-LP) conversions under both linearly and circularly polarized incidence. When the diodes are switched ON, the structure performs linear-to-cross-linear polarization conversion in the 9.5–16.4 GHz band and circular-to-co-circular polarization conversion in the 9.3–16.6 GHz band. Dual-band LP-CP and CP-LP conversions are attained in the 8.0–9.3/16.6–17.7 GHz and 8.1–9.4/16.8–17.9 GHz bands, respectively. When the diodes are OFF, the converter maintains co-polarized reflection under linearly polarized (LP) wave incidence, while reversing the handedness of the incident circularly polarized (CP) wave. Both full-wave simulations and experimental measurements demonstrate consistent performance across a broad bandwidth. This work provides a versatile and efficient solution for modern wireless communication and radar systems requiring adaptive polarization control.

1. INTRODUCTION

Polarization converters are of critical importance in radar and wireless communication systems. Conventional polarization conversion schemes typically rely on birefringent crystals or ferrite-based devices, which often suffer from large volume, difficulties in integration, and high losses [1, 2]. Metasurfaces, as two-dimensional artificial metamaterials, enable flexible manipulation of the amplitude, phase, and polarization properties of electromagnetic waves, offering a novel approach to polarization conversion [3–8]. Currently, metasurface-based polarization converters can be broadly categorized into two types: linear to orthogonal linear polarization (LP-OLP) and linear to circular polarization (LP-CP) [9–19]. However, most current designs remain passive and inherently static, which limits their deployment in modern systems requiring dynamic control capabilities.

To overcome this limitation, various reconfigurable polarization converters have been proposed [20–28]. Refs. [20–22] introduced a design capable of switching between LP-OLP and no conversion state. Ref. [23] demonstrated switchable LP-OLP and LP-CP states. To extend the operational bandwidth, Ref. [24] proposed a symmetric L-shaped patch metasurface unit, exciting multiple resonant modes to achieve ultra-wideband polarization control. Refs. [25, 26] realized LP-CP and dual-band LP-OLP conversion. Recently, [27] proposed a converter capable of switching among three modes (LP-OLP, LP-CP, and no conversion state). Despite these advancements, a critical limitation persists in most of these reconfigurable metasurfaces: they can only perform efficient polarization conversion under a single type of polarization incidence (typically linear). This significantly restricts their flexibility and adaptability in practical applications where the incident polarization state may be unknown or varying. Although the structure presented in Ref. [28] can achieve both co- and cross-polarized conversion for circularly polarized (CP) and linearly polarized (LP) incident waves, it still exhibits a limited operating bandwidth and supports merely two conversion modes. These shortcomings highlight a growing demand for broadband, multi-mode, and dynamically tunable polarization converters in next-generation wireless applications [29, 30].

In this paper, we propose a broadband reconfigurable polarization converter (BRPC) that addresses the aforementioned limitations by offering versatile functionality under both LP and CP incidence. The key advance of our design is its ability to dynamically switch among all fundamental polarization conversion states — including linear-to-linear (co- and cross-polarization), circular-to-circular (co- and cross-polarization), linear-to-circular (LP-CP), and circular-to-linear (CP-LP) conversions — depending on the bias state of the integrated PIN diodes. To experimentally validate the performance of the proposed metasurface structure, a prototype was fabricated and

* Corresponding author: Wei Li (liwei_seu@126.com).

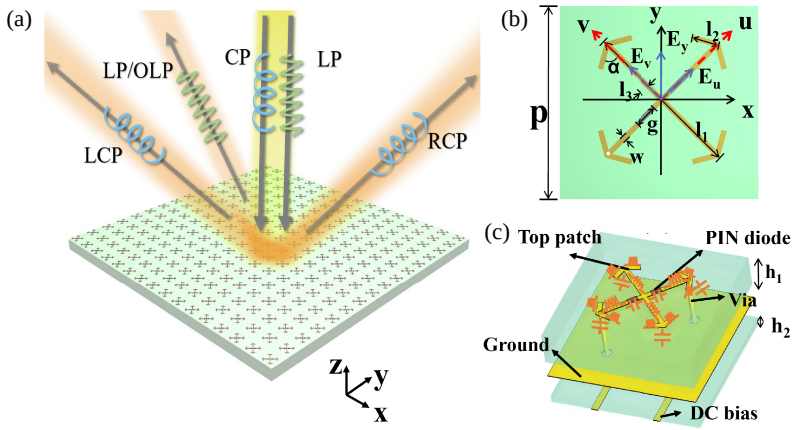

FIGURE 1. (a) Functional schematic of a reflective BRPC. (b) Top view of the unit cell. (c) Perspective view of the unit cell.

characterized, with measurement results showing good agreement with numerical simulations. Furthermore, the converter features a wide relative bandwidth and high conversion efficiency, demonstrating its promising potential for applications in modern communication systems.

2. THEORETICAL ANALYSIS AND DESIGN

To realize a fully functional reconfigurable polarization converter, it is essential to analyze its operating principle, which provides the theoretical basis for the subsequent design. As illustrated in Fig. 1, the metasurface can dynamically reconfigure the polarization state of the reflected wave across all possible linear and circular polarizations — regardless of whether the incident wave is linearly or circularly polarized — by switching the bias states of the PIN diodes. Taking, for example, a y-direction linearly polarized incident wave (Fig. 1(b)), it can be resolved into two orthogonal components along the u- and v-axes, which are oriented at $\pm 45°$ relative to the $+y$ direction, respectively. Accordingly, the x-polarized electric field of the incident wave can be expressed as:

$$\overrightarrow{E_{iy}} = \left(\sqrt{2}/2\right)\left(E_0 e^{jkz}\overrightarrow{u} + E_0 e^{jkz}\overrightarrow{v}\right). \tag{1}$$

The electric field of the reflected wave can be expressed as

$$\overrightarrow{E_r} = \left(\sqrt{2}/2\right)\left(E_0\left|r_{uu}\right| e^{-(jkz+\varphi_{uu})}\overrightarrow{u} + E_0\left|r_{vv}\right| e^{-(jkz+\varphi_{vv})}\overrightarrow{v}\right) \tag{2}$$

where $|r_{uu}|$ and $|r_{vv}|$ denote the reflection amplitudes under u- and v-polarized excitations, and φ_{uu}, φ_{vv} represent the corresponding phases, respectively.

According to Eq. (2), when the phase difference $\Delta\varphi = \varphi_{uu} - \varphi_{vv}$ equals $0°$, $\pm 90°$, or $180°$ and both $|r_{uu}|$ and $|r_{vv}|$ are close to 1, the reflected wave can be further expressed as follows:

$$\overrightarrow{E_r} = \begin{cases} \left(\sqrt{2}E_0/2\right)\left(\overrightarrow{u} + \overrightarrow{v}\right)e^{-jkz} & \Delta\varphi = 0° \\ \left(\sqrt{2}E_0/2\right)\left(\overrightarrow{u} - j\overrightarrow{v}\right)e^{-jkz} & \Delta\varphi = 90° \\ \left(\sqrt{2}E_0/2\right)\left(\overrightarrow{u} + j\overrightarrow{v}\right)e^{-jkz} & \Delta\varphi = -90° \\ \left(\sqrt{2}E_0/2\right)\left(\overrightarrow{u} - \overrightarrow{v}\right)e^{-jkz} & \Delta\varphi = 180° \end{cases}. \tag{3}$$

Eq. (3) indicates that when the phase difference $\Delta\varphi$ equals $0°$, co-polarized maintenance is achieved under y-polarized incidence; when $\Delta\varphi$ equals $90°$, the reflected wave under y-polarized incidence is converted to an right-hand circularly polarized (RCP) wave; when $\Delta\varphi$ equals $-90°$, the reflected wave under y-polarized incidence is converted to an left-hand circularly polarized (LCP) wave; and when the phase difference $\Delta\varphi$ equals $180°$, the y-polarized incident wave is converted to cross-polarization. Similarly, analogous conclusions can be drawn for x-polarized incident waves.

Furthermore, assuming an RCP incident wave propagating along the $-z$ direction, its electric field can be decomposed into two linearly polarized components with equal amplitude and a $90°$ phase difference:

$$\overrightarrow{E_{iR}} = \left(\sqrt{2}/2\right)\left(E_0 e^{jkz}\overrightarrow{u} + jE_0 e^{jkz}\overrightarrow{v}\right). \tag{4}$$

Similarly, the reflected electric field is expressed as:

$$\overrightarrow{E_r} = \begin{cases} \left(\sqrt{2}E_0/2\right)\left(\overrightarrow{u} + j\overrightarrow{v}\right)e^{-jkz} & \Delta\varphi = 0° \\ \left(\sqrt{2}E_0/2\right)\left(\overrightarrow{u} + \overrightarrow{v}\right)e^{-jkz} & \Delta\varphi = 90° \\ \left(\sqrt{2}E_0/2\right)\left(\overrightarrow{u} - \overrightarrow{v}\right)e^{-jkz} & \Delta\varphi = -90° \\ \left(\sqrt{2}E_0/2\right)\left(\overrightarrow{u} - j\overrightarrow{v}\right)e^{-jkz} & \Delta\varphi = 180° \end{cases} \tag{5}$$

Eq. (5) indicates that when the phase difference $\Delta\varphi$ equals $0°$, the spin state of the reflected wave under RCP incidence is reversed, resulting in LCP waves due to the reversal of the propagation direction of the reflected wave. When $\Delta\varphi$ equals $90°$, the reflected wave under RCP incidence is converted to a y-polarized wave. When $\Delta\varphi$ equals $-90°$, the reflected wave under RCP incidence is converted to an x-polarized wave.

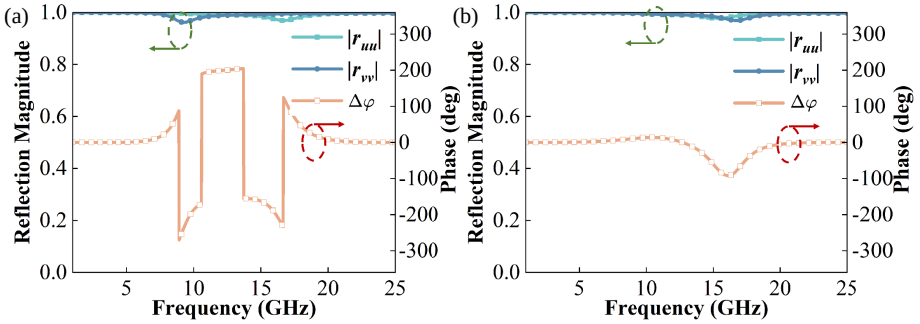

FIGURE 2. Reflection amplitudes and phase difference for the u- and v-polarized incident wave with the PIN diode in the (a) ON state and (b) OFF state.

When the phase difference $\Delta\varphi$ equals 180°, although the phase in the v-direction advances, the polarization of the reflected wave remains unchanged, again owing to the reversal of the propagation direction. Similarly, analogous conclusions can be drawn for LCP incident waves. Thus, for an LP incident wave, the metasurface enables conversion to co-polarized, cross-polarized, and CP states. Similarly, for a CP incident wave, it facilitates conversion to co-polarized, cross-polarized, and LP states.

The proposed wideband reconfigurable polarization converter, designed based on the above theoretical principles, is depicted in Fig. 1(c). The architecture consists of three metallic layers separated by dielectric substrates. On the top layer, two arrow-headed patches are arranged symmetrically along the unit cell's diagonal, incorporating two slots aligned with the u-direction. PIN diodes are mounted across these slots and electrically connected to the top metal patterns. The middle layer serves as a solid metal ground plane, providing complete reflection of incident waves. A DC bias network is integrated on the bottom layer to control the PIN diodes. The dielectric substrate is made of FR4 material with a relative permittivity of 4.4 and a loss tangent of 0.02. After structural optimization, the final geometric parameters of the unit cell are determined as follows: $h_1 = 4\,\text{mm}$, $h_2 = 0.8\,\text{mm}$, $P = 9\,\text{mm}$, $l_1 = 6\,\text{mm}$, $l_2 = 1\,\text{mm}$, $l_3 = 0.5\,\text{mm}$, $w = 0.3\,\text{mm}$, $g = 0.9\,\text{mm}$, $\alpha = 60°$. As illustrated in Fig. 1(b), h_1 denotes the thickness of the upper dielectric substrate; h_2 represents the thickness of the lower dielectric substrate; P is the periodicity of the unit cell; l_1 corresponds to the length of the metal arrow-head patch; l_2 indicates the length of the arrow-tail segment; w defines the width of the metal pattern; g refers to the gap length between adjacent structures; and α signifies the angle between the arrow tail and the main body. The PIN diodes used are the SMP1320-079LF from Skyworks.

3. SIMULATION AND ANALYSIS

To validate whether the designed metasurface satisfies the theoretical performance targets, electromagnetic simulations of the BRPC were carried out in CST Microwave Studio. Unit cell boundary conditions were applied along the x- and y-directions, while a Floquet port was used to excite the structure in the z-direction. The simulated reflection amplitudes and phase differences in the uv-coordinate system are presented. When the diodes are in the ON state, the results in Fig. 2(a) show that $|r_{uu}|$ and $|r_{vv}|$ are nearly unity across the operating band, indicating low loss in the PCM. The phase difference approaches 90° in the 8.5–9.3 GHz and 16.6–17.7 GHz bands, yielding well-performing circularly polarized reflection. Additionally, the phase difference nears 180° at 9.5–16.4 GHz, achieving ideal cross-polarization conversion. When the diodes are in OFF state, as shown in Fig. 2(b), $|r_{uu}|$ and $|r_{vv}|$ remain close to 1, but the phase difference is approximately 0° throughout the simulated band, resulting in perfect co-polarized conversion.

The reflection coefficients for y-polarized LP and RCP incident waves on the reference plane are defined as follows:

$$r_{yy} = E_{ry}/E_{iy}, \quad r_{xy} = E_{rx}/E_{iy} \tag{6}$$

$$r_{RR} = E_{rR}/E_{iR}, \quad r_{LR} = E_{rL}/E_{iR} \tag{7}$$

where r_{yy} and r_{xy} denote the co-polarized and cross-polarized reflection coefficients under y-polarized incidence, where E_{ry} and E_{rx} represent the reflected y- and x-polarized electric fields, respectively, and E_{iy} is the incident y-polarized electric field. Similarly, r_{RR} and r_{LR} correspond to the co-polarized and cross-polarized reflection coefficients under RCP incidence; E_{rR} and E_{rL} refer to the reflected RCP and LCP electric fields, respectively, while E_{iR} signifies the incident RCP electric field.

The polarization conversion ratio (PCR), defined as $\text{PCR} = r_{xy}^2/(r_{xy}^2 + r_{yy}^2)$, quantifies the effectiveness of polarization conversion. For y-polarized incident waves, the efficiency of circular polarization conversion is evaluated using the axial ratio (AR), given by:

$$\text{AR} = \left(\frac{|r_{xy}|^2 + |r_{yy}|^2 + \sqrt{a}}{|r_{xy}|^2 + |r_{yy}|^2 - \sqrt{a}} \right)^{1/2} \tag{8}$$

where

$$a = |r_{xy}|^4 + |r_{yy}|^4 + 2\,|r_{xy}|^2\,|r_{yy}|^2 \cos(2\Delta\varphi). \tag{9}$$

When PIN diodes are in the ON state, the amplitudes and phase differences of the co-polarized and cross-polarization reflections under y-polarized incident waves are shown in Fig. 3(a). It is observed that r_{xy} is greater than $-1\,\text{dB}$ in the range of 9.5–16.4 GHz, while r_{yy} is below $-13\,\text{dB}$, indicating that the y-polarized incident wave is largely con-

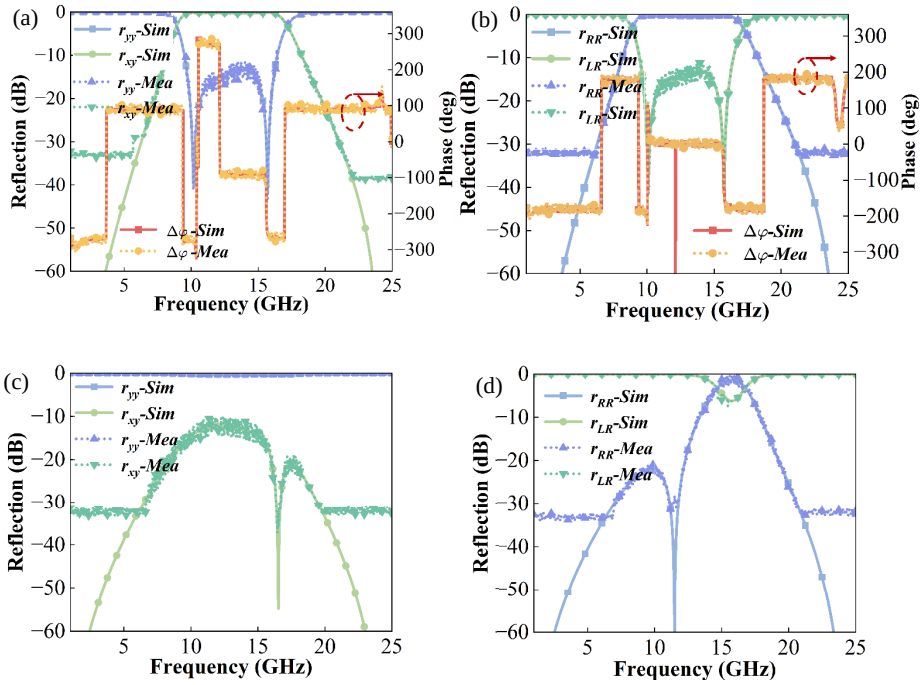

FIGURE 3. Numerical and measurement results: (a) y-polarized wave in the ON state; (b) RCP wave in the ON state; (c) y-polarized wave in the OFF state; (d) RCP wave in the OFF state.

verted to a cross-polarization reflection. Simultaneously, in the 8.0–9.3 GHz and 16.6–17.7 GHz bands, the reflection coefficients r_{xy} and r_{yy} are equal, and the phase difference $\Delta\varphi = \varphi_{xy} - \varphi_{yy}$ is approximately 90°, signifying that the converter achieves LP-CP conversion. Fig. 3(b) illustrates the simulated reflection amplitude and phase under RCP wave excitation. The results exhibit a notable similarity to those obtained under y-polarized wave excitation. Within the frequency range of 9.3–16.6 GHz, the reflected wave maintains a co-polarized state. Furthermore, Within the frequency bands of 8.4–9.1 GHz and 16.8–17.6 GHz, the incident and reflected waves exhibit equal amplitude and a 180° phase difference. As a result, they combine to form an LP wave, achieving CP-LP conversion.

When PIN diodes are in the OFF state, the simulated reflection amplitudes under y-polarized and RCP wave excitation are presented in Figs. 3(c) and 3(d), respectively. It can be observed that within the frequency range of 1 to 25 GHz, r_{yy} is greater than -1 dB, while r_{xy} remains below -11 dB. This indicates that the y-polarized incident wave is predominantly converted to a co-polarized reflected wave. Similarly, r_{LR} exceeds -1 dB within both the 1–14 GHz and 17–25 GHz bands, indicating that the incident RCP wave is converted to an LCP wave upon reflection. Owing to the structural symmetry along the u-axis, the simulated results are identical for both x- and y-polarized incidences, as well as for LCP and RCP excitations.

Figures 4(a) and (b) present the simulated cross-polarization reflection coefficient r_{xy} when the PIN diodes are switched ON, and the co-polarization reflection coefficient r_{yy} when the diodes are OFF, respectively, as functions of the parameter l_1. It can be observed that increasing the dimension l_1 enhances the conversion efficiency; however, this is accompanied by a gradual reduction in operating bandwidth. After a comprehensive parameter sweep and optimization process, l_1 was ultimately determined to be 6 mm. Furthermore, Figs. 4(c) and (d) display the corresponding variations in r_{xy} and r_{yy} with respect to the parameter w. A clear optimum for efficiency is evident at $w = 0.3$ mm. Considering this performance peak alongside practical fabrication constraints, w was consequently finalized at 0.3 mm.

To validate the angular stability of the proposed structure, Fig. 5(a) presents the simulated PCR under y-polarized wave incidence at angles of 0°, 15°, and 30° when the PIN diodes are in the ON state. The PCR exceeds 90% within the 9.6–16.3 GHz frequency range. Furthermore, it can be observed that the PCR for LP-OLP conversion is insensitive to the oblique incidence angle — even when the angle of incidence increases to 30°, the bandwidth over which the PCR exceeds 90% remains largely unchanged. The calculated AR under y-polarized wave is shown in Fig. 5(b). The results demonstrate that the AR remains below 3 dB across two broad frequency bands, 8–9.3 GHz and 16.6–17.7 GHz. The AR also exhibits stability under various incidence angles, indicating relatively high angular stability of the BRPC.

Correspondingly, the PCR under RCP wave incidence is shown in Fig. 5(c). Similarly, the PCR remains stable under different angles of wave incidence. From Fig. 5(d), it can be observed that the AR exceeds 20 dB within the frequency bands of 8.1–9.4 GHz and 16.8–17.9 GHz, indicating that the power density of the larger LP component significantly exceeds that of the smaller LP component [31]. Thus, the reflected wave can be regarded as LP, confirming the achievement of CP-LP conversion. The angular stability of the BRPC primarily arises from the subwavelength design and the electrically thin profile

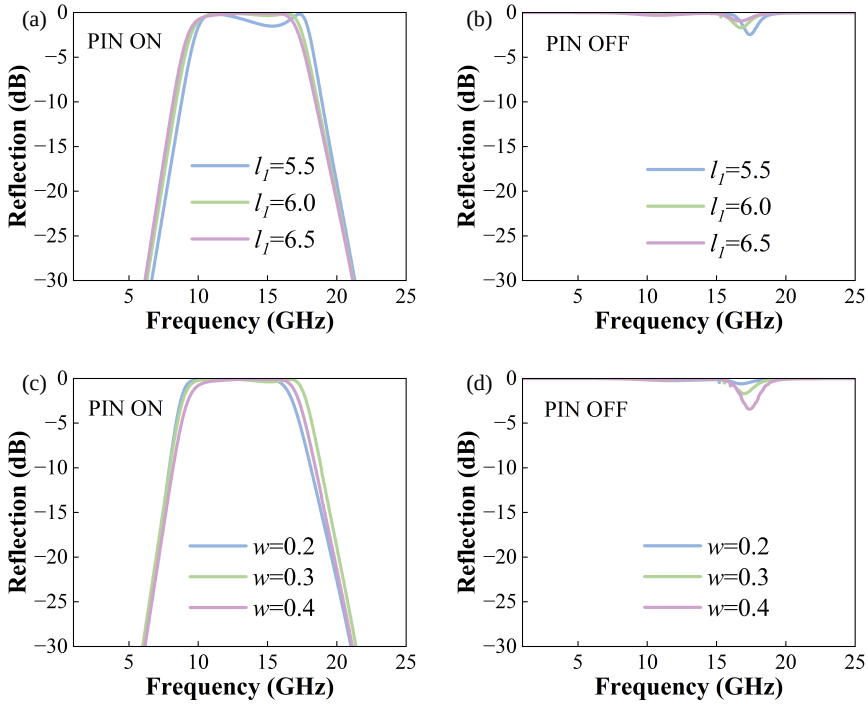

FIGURE 4. Parametric studies of key dimensions. (a) r_{xy} vs. l_1 (ON-state), (b) r_{yy} vs. l_1 (OFF-state), (c) r_{xy} vs. w (ON-state), and (d) r_{yy} vs. w (OFF-state).

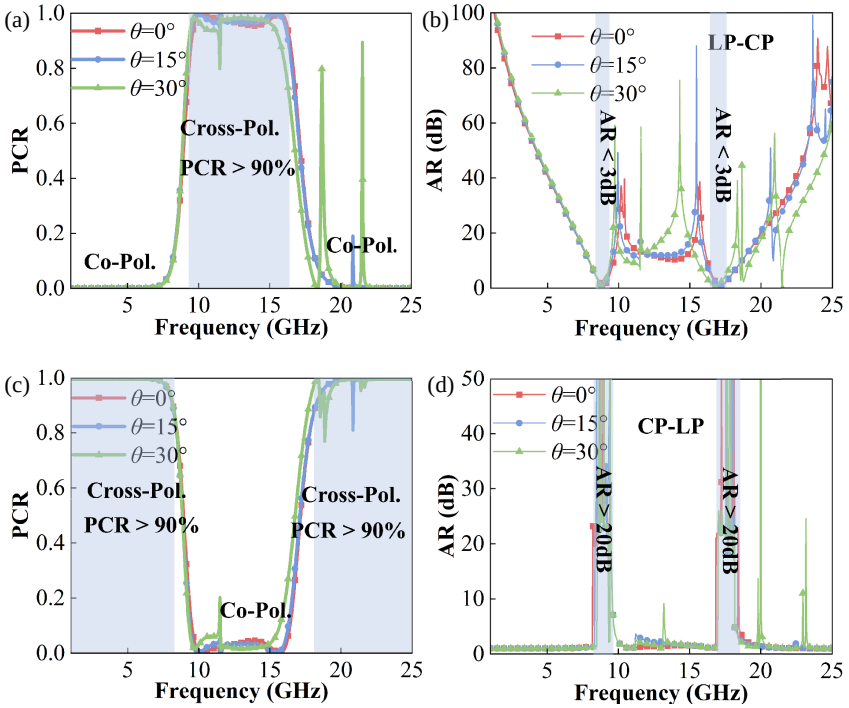

FIGURE 5. Simulated performance under different excitations and incidence angles: (a) PCR under y-polarized incidence; (b) AR under y-polarized incidence; (c) PCR under RCP incidence; (d) AR under RCP incidence.

of the unit cell, which avoids introducing significant additional phase accumulation under oblique incidence.

Figure 6 displays the current density distributions in the ON state of the diodes at resonant frequencies of 9 GHz, 14.4 GHz, 15.6 GHz, and 17.2 GHz. As depicted in Fig. 6(a), at 9 GHz, the equivalent currents (indicated by red arrows) in the first and second sections flow along two orthogonal diagonal directions, giving rise to a CP reflected wave. In Fig. 6(b), at 14.4 GHz along the v-direction, anti-parallel current alignment is observed between the top layer (red arrows) and the bot-

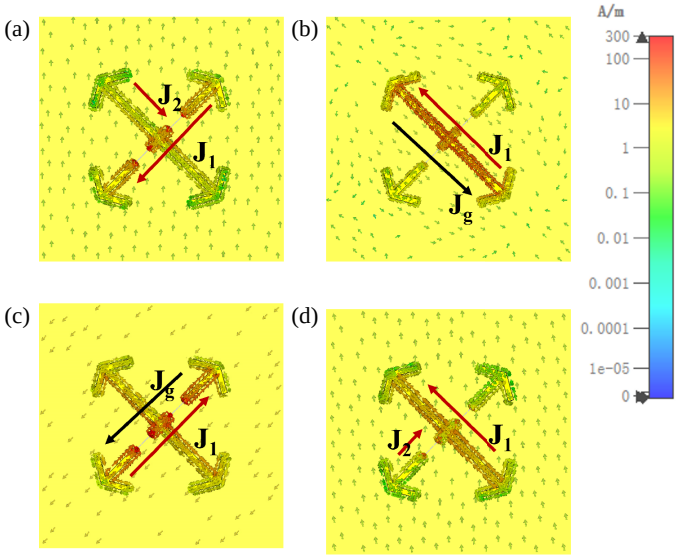

FIGURE 6. Induced surface current distribution under a y-polarized incident wave at (a) 9 GHz, (b) 14.4 GHz, (c) 15.6 GHz and (d) 17.2 GHz.

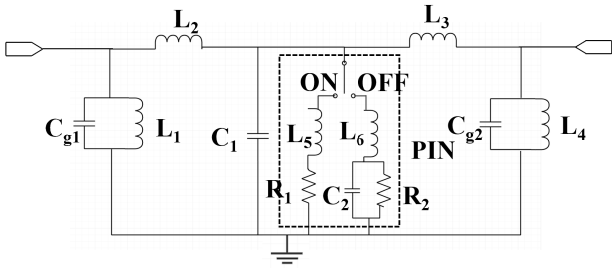

FIGURE 7. Equivalent circuit of the BRPC. $C_{g1} = C_{g2} = 0.025$ pF, $C_1 = 0.009$ pF, $L_2 = L_3 = 2.39$ nH, $L_1 = L_4 = 1.32$ nH, $R_1 = 0.41\,\Omega$, $L_5 = 0.7$ nH, $L_6 = 40$ nH, $C_2 = 0.4$ pF, $R_2 = 400\,\text{k}\Omega$.

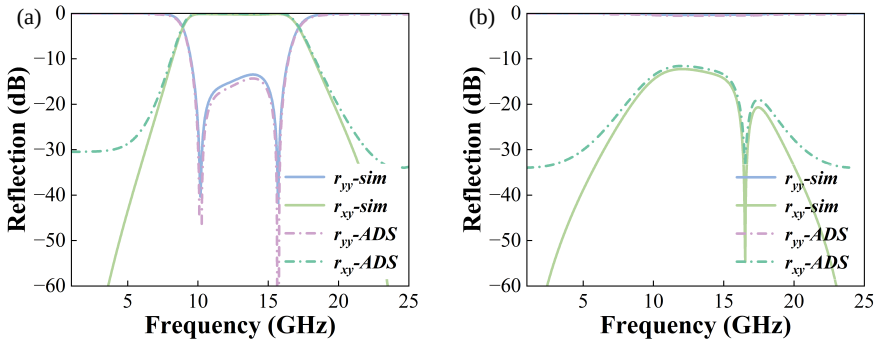

FIGURE 8. Results simulated by CST and ADS. (a) PIN in the ON state. (b) PIN in the OFF state.

tom layer (black arrows), exciting a magnetic dipole resonance along the u-direction. This resonance significantly enhances the equivalent permeability for the u-component of the electric field, resulting in a high-impedance surface that introduces a 180° phase reversal in the reflected u-polarized electric field relative to the incident wave. By contrast, no resonant behavior occurs along the v-direction, where the v-polarized reflection remains in-phase with the incident field. Consequently, the overall reflected wave at 14.4 GHz becomes x-polarized. Similarly, cross-polarized and circularly polarized reflections are achieved at 15.6 GHz and 17.2 GHz, respectively.

To further elucidate the mechanism underlying electromagnetic wave manipulation in the proposed structure, an equivalent circuit model is developed for the active metasurface. In this model, the inter-patch gaps are represented as capacitive elements, whereas the metallic patches are characterized as inductive components, as shown in Fig. 1(c). The derived equivalent circuit, shown in Fig. 7, reveals that the reflection coefficient can be dynamically tuned by altering the switching states of the integrated PIN diodes. In ADS software, the equivalent circuit shown in Fig. 7 was constructed, and the component values of each circuit element were obtained by fitting the electromagnetic simulation curves from CST software, as illustrated in the figure.

Figure 8 shows the comparison of reflection coefficients between the equivalent circuit and CST full-wave simulation results. Fig. 8(a) presents the reflection coefficients when the diode is in the ON state, while Fig. 8(b) displays the results when the diode is in the OFF-state. The close agreement between the two sets of results validates that controlling the diode states can effectively modulate the reflection coefficients, thereby enabling the polarization conversion functionality.

4. FABRICATION AND MEASUREMENT

To validate the simulation results, a prototype consisting of 16×16 unit cells was manufactured via printed circuit board (PCB) technology and subjected to performance measurement. The overall dimensions of the sample measure $144\,\text{mm} \times 144\,\text{mm} \times 4.8\,\text{mm}$, as illustrated in Fig. 9(a). The DC bias lines, etched on the back side of the board as shown in Fig. 9(b), form the foundation of the biasing network. To ensure effective RF-DC

TABLE 1. Comparison with previous works.

Ref.	IP	PCP	RB (GHz)	AS (°)
[23]	LP	i) Cross-Pol. ii) LP-CP	i) 10.5–13.9(27.9%)/17.7–27.2(42.3%) ii) 11.8–24.1(68.5%)	N/A
[26]	LP	i) Cross-Pol. ii) LP-CP	i) 7.30–8.90(19.7%)/19.40–24.92(24.8%)/8.9–13.22(37.5%) ii) 9.79–17.42(55.8%)/7.60–8.30(8.8%)/14.71–16.83(13.3%)	N/A
[27]	LP	i) Cross-Pol. ii) LP-CP iii) Co-Pol.	i) 3.77–6.20(48.8%) ii) 5.2–6.1(16%)/7.75–8.6(10.4%) iii) 2–3.66(58.7%)/8.42–9.52(13.3%)	10
[28]	LP/CP	i) Co-Pol. ii) Cross-Pol.	7.4–12(47.4%) for CP and LP.	20
This work	**LP/CP**	i) Cross-Pol. ii) Co-Pol. **iii) LP-CP** **iv) CP-LP**	i) 9.5–16.4(53.3%) for LP; 1–14(173.3%) and 17–25(38.1%) for CP. ii) 1–25(184.6%) for LP; 9.3–16.6(56.3%) for CP. iii) 8.0–9.3(15.0%)/16.6–17.7(6.4%) iv) 8.1–9.4(14.8%)/16.8–17.9(6.3%)	30

IP: Incident Polarization, PCP: Polarization Conversion Property,
RB: Relative Bandwidth of PCR > 0.9 or AR < 3 dB. AS: Angular Stability.

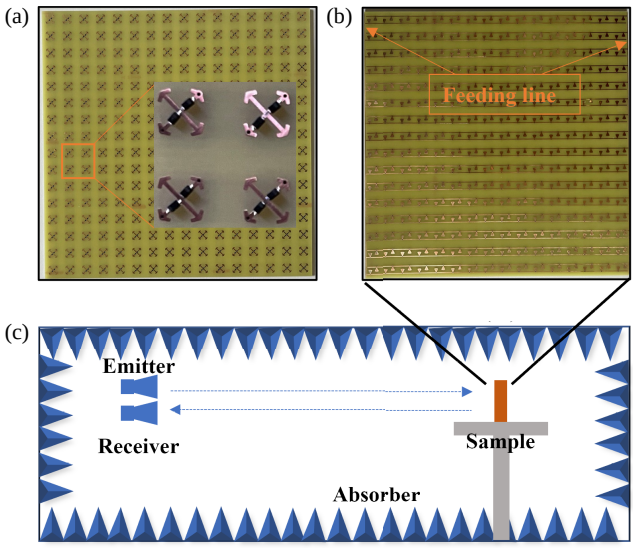

FIGURE 9. Fabricated sample of BRPC. (a) Top layer, (b) biasing arrangement of bottom layer, and (c) schematic diagram for measurement setup.

isolation, this design incorporates radial stub filters at the critical connection points on the bottom layer. These strategically placed filters effectively suppress high-frequency signal leakage into the DC paths, thus preserving the system's RF performance while maintaining precise bias control through the implemented AC/DC isolation techniques. A schematic of the measurement setup is illustrated in Fig. 9(c). To minimize interference from scattered electromagnetic waves, the area surrounding the sample was covered with absorbing material. Due to the broadband characteristics of the proposed structure, two sets of horn antennas were utilized during the experiment, covering frequency bands of 1–18 GHz and 18–26 GHz, with maximum gains of 14 dBi and 20 dBi, respectively. To ensure that the sample was located in the far-field region of the horn antennas, the far-field condition $R = 2D^2/\lambda$ was applied. By incorporating the electrical size of the sample and the operating wavelength, the maximum required distance R was calculated to be 4.8 m. In the experiment, the distance between the sample and the horn antenna was set to 5 m. Meanwhile, the reflection coefficient of an equal-sized metal plate was measured to normalize the reflection coefficient of the metasurface.

Figure 3 shows the measured reflection coefficients of the PIN diode under two states (ON/OFF) for both LP and CP incident waves. When all diodes are in the ON state, the designed sample under y-polarized LP wave excitation exhibits a reflection coefficient greater than -1 dB within the frequency range of 9.4–16.5 GHz, achieving cross-polarization conversion. In the frequency bands of 8.0–9.2 GHz and 16.7–17.6 GHz, nearly equal amplitude is observed, enabling LP-CP conversion. Similarly, under RCP wave incidence, the sample maintains co-polarized conversion from 9.5–16.2 GHz, while CP-LP conversion is accomplished in the ranges of 8.5–9.4 GHz and 16.5–17.3 GHz.

In contrast, when all diodes are switched to the OFF state, the sample functions as a co-polarization converter under y-polarized LP wave excitation across the entire 1–25 GHz band. Under RCP incidence, it operates as a cross-polarization converter in the frequency ranges of 1–13.8 GHz and 17.2–25 GHz. The experimental results show strong consistency with the simulated data, confirming the feasibility of the polarization-reconfigurable conversion strategy presented in this work. Slight deviations observed between the two are mainly due to fabrication and measurement tolerances.

Table 1 presents a comprehensive performance comparison between the proposed converter and prior works. This comparison reveals that our design achieves a superior integration of functionality, bandwidth, and angular stability. While most predecessors are limited to LP incidence and fewer functional modes, our device operates effectively under both LP and CP

waves, providing four distinct switching states. More notably, it exhibits wideband responses while simultaneously maintaining robust performance under oblique incidence up to 30°, a significant improvement in angular stability over existing solutions. This combination of multi-polarization incidence support, diverse functionality, wide bandwidth, and excellent angular stability underscores the practical superiority of our design.

5. CONCLUSION

In summary, a fully functional BRPC has been developed using an active metasurface integrated with PIN diodes. A key achievement of this work is the demonstration of full polarization manipulation under both linear and circular polarized incidence. When the diodes are switched ON, an LP incident wave is converted to a CP reflected wave in the 8.0–9.3 GHz and 16.6–17.7 GHz bands, and to a cross-polarized wave in the 9.5–16.4 GHz band. Correspondingly, under CP incidence, LP and co-polarized reflected waves are obtained within the similar bands, with an effective bandwidth comparable to that under LP excitation. When the diodes are switched OFF, the polarization of an LP wave remains unchanged, while the handedness of an incident CP wave is reversed. Measured results closely match the simulated performance, validating the feasibility of the proposed BRPC and supporting its potential use in wireless communication systems.

ACKNOWLEDGEMENT

This study was supported by the National Natural Science Foundation of China (62201136, 62288101), the Research Foundations of Science and Technology on Antenna and Microwave Laboratory (6142402220304), Jiangsu Province 333 High-level Talent Cultivation Project, Jiangsu Province Young Teachers Enterprise Practice Program (2025QYSJ104), Natural Science Foundation of Jiangsu College of Engineering and Technology (JSGYZRJJYB-07).

REFERENCES

[1] Zhuang, Z., S.-W. Suh, and J. S. Patel, "Polarization controller using nematic liquid crystals," *Optics Letters*, Vol. 24, No. 10, 694–696, 1999.

[2] Fu, H. and R. E. Cohen, "Polarization rotation mechanism for ultrahigh electromechanical response in single-crystal piezoelectrics," *Nature*, Vol. 403, No. 6767, 281–283, 2000.

[3] Shelby, R. A., D. R. Smith, and S. Schultz, "Experimental verification of a negative index of refraction," *Science*, Vol. 292, No. 5514, 77–79, 2001.

[4] Larouche, S., Y.-J. Tsai, T. Tyler, N. M. Jokerst, and D. R. Smith, "Infrared metamaterial phase holograms," *Nature Materials*, Vol. 11, 450–454, 2012.

[5] Cui, T.-J., S. Liu, and L.-L. Li, "Information entropy of coding metasurface," *Light: Science & Applications*, Vol. 5, e16172, 2016.

[6] Li, L., H. Zhao, C. Liu, L. Li, and T. J. Cui, "Intelligent metasurfaces: Control, communication and computing," *eLight*, Vol. 2, No. 1, 7, 2022.

[7] Djoudi, M., M. L. Tounsi, J. Sarrazin, and M. Casaletti, "Efficient design of a novel multibeam antenna using scalar metasurfaces," *Progress In Electromagnetics Research*, Vol. 183, 9–20, 2025.

[8] Li, F., T. Pan, W. Li, Z. Peng, D. Guo, X. Jia, T. Hu, L. Wang, W. Wang, M. Gao, *et al.*, "Flexible intelligent microwave metasurface with shape-guided adaptive programming," *Nature Communications*, Vol. 16, No. 1, 3161, Apr. 2025.

[9] Zhou, E., Y. Cheng, F. Chen, H. Luo, and X. Li, "Low-profile high-gain wideband multi-resonance microstrip-fed slot antenna with anisotropic metasurface," *Progress In Electromagnetics Research*, Vol. 175, 91–104, 2022.

[10] Xu, Z., C. Ni, Y. Cheng, L. Dong, and L. Wu, "Photo-excited metasurface for tunable terahertz reflective circular polarization conversion and anomalous beam deflection at two frequencies independently," *Nanomaterials*, Vol. 13, No. 12, 1846, 2023.

[11] You, X., R. T. Ako, M. Bhaskaran, S. Sriram, C. Fumeaux, and W. Withayachumnankul, "Mechanically tunable terahertz circular polarizer with versatile functions," *Laser & Photonics Reviews*, Vol. 17, No. 4, 2200305, 2023.

[12] Zhu, W., Y. Fan, R. Yang, H. Zhao, G. Geng, X. Guo, P. Li, Q. Fu, K. Sun, C. Gu, Y. Zhang, J. Li, and F. Zhang, "Full-space and arbitrary orbital angular momentum multiplexed beam manipulation with a titanium dioxide metadevice," *Nano Letters*, Vol. 25, No. 39, 14 237–14 245, 2025.

[13] Huang, Z., Z. Wang, Y. Cheng, X. Li, J. Wang, L. Zhou, H. Xu, X. Luo, and L. Chen, "Metasurfaces empower optical multiparameter imaging: A review," *Science China Physics, Mechanics & Astronomy*, Vol. 68, 274201, 2025.

[14] Wang, J., L. Yang, B. Cai, Y. Cheng, and X. Li, "Ultra-broadband tunable terahertz chiral metasurface integrated vanadium dioxides for tri-functional application," *Physica E: Low-dimensional Systems and Nanostructures*, Vol. 172, 116270, 2025.

[15] Rong, C., L. Wu, J. Tao, Y. Cheng, K. Wang, L. Chen, H. Luo, F. Chen, and X. Li, "Metasurface-based optical neural network and its application in next-generation optical communications and networks," *Journal of Lightwave Technology*, Vol. 43, No. 18, 8538–8562, 2025.

[16] Wang, J., Y. Xiao, L. Yang, D. Wang, B. Cai, H. Luo, and Y. Cheng, "Dual-controlled terahertz tunable broadband metasurface based on photosensitive silicon and vanadium dioxide for multi-functional application," *Physics Letters A*, Vol. 556, 130841, 2025.

[17] Wang, S.-Y., J.-D. Bi, W. Liu, W. Geyi, and S. Gao, "Polarization-insensitive cross-polarization converter," *IEEE Transactions on Antennas and Propagation*, Vol. 69, No. 8, 4670–4680, 2021.

[18] Faraz, Z., B. Kamal, S. Ullah, A. Aziz, and H. Kanwal, "High efficient and ultra-wideband polarization converter based on I-shaped metasurface for RCS reduction," *Optics Communications*, Vol. 530, 129101, 2023.

[19] Bo, X.-Z., H. Chen, B.-Y. Yu, M.-Y. Geng, Z.-G. Liu, and W.-B. Lu, "A flexible and transparent broadband metasurface polarization converter," *IEEE Antennas and Wireless Propagation Letters*, Vol. 23, No. 4, 1311–1315, 2024.

[20] Li, Y., Y. Wang, and Q. Cao, "Design of a multifunctional reconfigurable metasurface for polarization and propagation manipulation," *IEEE Access*, Vol. 7, 129 183–129 191, 2019.

[21] Wang, S.-Y., W. Liu, and W. Geyi, "A circular polarization converter based on in-linked loop antenna frequency selective surface," *Applied Physics B*, Vol. 124, 126, 2018.

[22] Li, W., S. Xia, B. He, J. Chen, H. Shi, A. Zhang, Z. Li, and Z. Xu, "A reconfigurable polarization converter using active metasur-

face and its application in horn antenna," *IEEE Transactions on Antennas and Propagation*, Vol. 64, No. 12, 5281–5290, 2016.

[23] Sun, S., W. Jiang, S. Gong, and T. Hong, "Reconfigurable linear-to-linear polarization conversion metasurface based on PIN diodes," *IEEE Antennas and Wireless Propagation Letters*, Vol. 17, No. 9, 1722–1726, 2018.

[24] Yang, H., S. C. Wang, P. Li, Y. He, and Y. J. Zhang, "A broadband multifunctional reconfigurable polarization conversion metasurface," *IEEE Transactions on Antennas and Propagation*, Vol. 71, No. 7, 5759–5767, 2023.

[25] Yang, Z., N. Kou, S. Yu, F. Long, L. Yuan, Z. Ding, and Z. Zhang, "Reconfigurable multifunction polarization converter integrated with pin diode," *IEEE Microwave and Wireless Components Letters*, Vol. 31, No. 6, 557–560, 2021.

[26] Guo, Q., F. Hao, M. Qu, J. Su, and Z. Li, "Multiband multifunctional polarization converter based on reconfigurable metasurface," *IEEE Antennas and Wireless Propagation Letters*, Vol. 23, No. 4, 1241–1245, 2024.

[27] Pramanik, S., S. C. Bakshi, C. Koley, D. Mitra, A. Monti, and F. Bilotti, "Active metasurface-based reconfigurable polarization converter with multiple and simultaneous functionalities," *IEEE Antennas and Wireless Propagation Letters*, Vol. 22, No. 3, 522–526, 2023.

[28] Liu, W., J. C. Ke, C. Xiao, L. Zhang, Q. Cheng, and T. J. Cui, "Broadband polarization-reconfigurable converter using active metasurfaces," *IEEE Transactions on Antennas and Propagation*, Vol. 71, No. 4, 3725–3730, 2023.

[29] Bhattacharjee, A. and S. Dwari, "Design of an anisotropic reconfigurable reflective polarization converter for realizing circular polarization-reconfigurable antenna," *IEEE Antennas and Wireless Propagation Letters*, Vol. 21, No. 12, 2392–2396, 2022.

[30] Zhu, S. S., P. Wang, Y. Zhang, Z. M. Yan, Y. Wang, and H. C. Zhou, "A reconfigurable polarization converter and related application as horn antenna cladding," *Journal of Applied Physics*, Vol. 133, No. 2, 023102, 2023.

[31] Lin, B., W. Huang, J. Guo, Y. Wang, Z. Liu, and H. Ye, "A high efficiency ultra-wideband circular-to-linear polarization conversion metasurface," *Optics Communications*, Vol. 529, 129102, 2023.